EPJ manuscript No.
(will be inserted by the editor)

Status of ATLAS and Expectations for First Physics At The LHC

Arno Straessner[1,a], on behalf of the ATLAS Collaboration.

Université de Genève, Switzerland; now with: Technische Universität Dresden, Germany

Abstract. We report on the status of the ATLAS experiment at the LHC. Expectations for first data taking in 2009 and the following years are presented. After an overview of the LHC collider commissioning, the ATLAS detector performance in test runs is shown. The physics road-map starts with early data analyses of Standard Model processes, like the measurement of W and Z production cross-sections at highest *pp* centre-of-mass energies. Interesting physics with single top and top-pairs including top mass determination are expected as well for the 2010 run. The main purpose of ATLAS is the search for new physics. Already in early data, the sensitivity is high for heavy partners of the vector bosons, W' and Z'. With more luminosity, the Standard Model and super-symmetric Higgs bosons come into reach. Expectations for a discovery in a few inverse femtobarn of data will be shown. Finally, the inclusive search for super-symmetric (SUSY) signatures and the anticipated coverage of the parameter space in mSUGRA and GMSB models are presented.

ATL-GEN-PROC-2009-001
06 January 2009

1 Introduction

The ATLAS [1] experiment is a multi-purpose physics detector at the Large Hadron Collider [2] (LHC) at CERN. The physics that shall be explored in proton-proton collisions at 14 TeV reaches from searches for new physics phenomena, like the Standard Model Higgs boson or super-symmetric particles, to measurements of Standard Model (SM) processes. Electroweak gauge bosons and top quarks are studied and precision physics, like the measurement of W boson and top quark masses, will be performed. When running at the LHC design luminosity of $\mathcal{L} = 10^{34}\text{cm}^{-1}\text{s}^{-1}$ about 100 fb^{-1} of data are expected per year and experiment. Rare processes requiring optimal detector performance can be searched for in this era. However, the high luminosity running will begin only after about 3 years of LHC operation and upgrade of the beam collimation system. This article is therefore concentrating on the current status of ATLAS and the LHC and expectations for the initial phase of ATLAS in the years 2009 and 2010.

2 The LHC and the start-up program

The LHC is installed in an underground tunnel and accelerates bunches of protons in a ring of 26.6 km circumference from the injection energy of 450 GeV to the nominal beam energy of 7 TeV. Figure 1 shows the LHC underground installation. In nominal operation, 2808 bunches, each containing $1.15 \cdot 10^{11}$ protons, are circulating in both directions of the LHC ring. The bunches are separated in time by 25 ns intervals.

[a] e-mail: Arno.Straessner@cern.ch

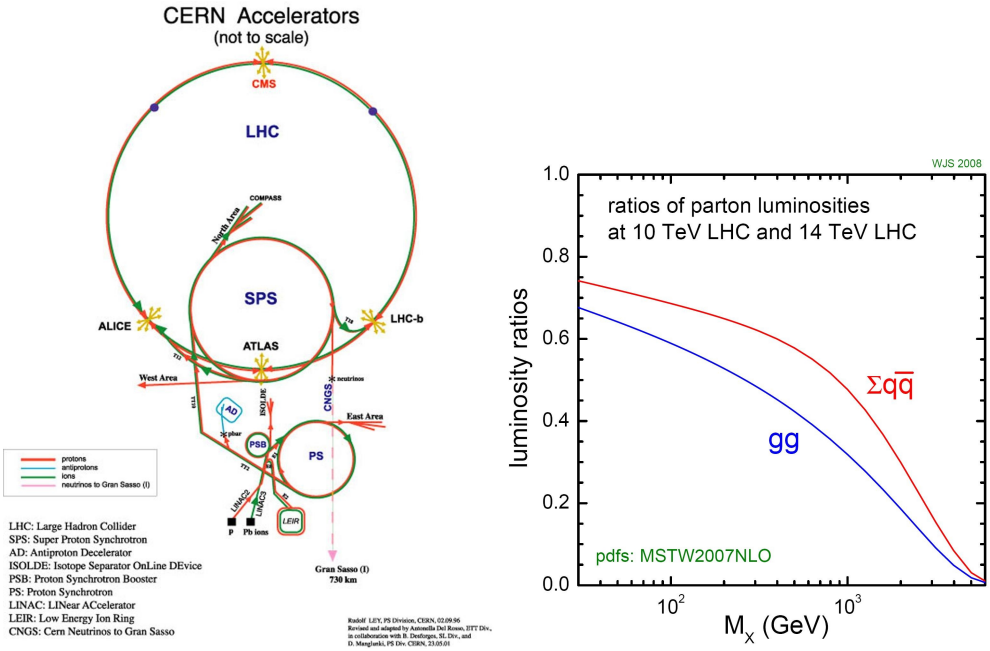

Fig. 1. a) The CERN accelerator complex. The ATLAS and CMS experiments are installed at opposite sites of the main LHC ring at access points 1 and 5. ALICE and LHCb are close to the ATLAS site at point 2 and 8, respectively. b) Ratio of parton luminosities for 10 TeV and 14 TeV centre-of-mass energies.

There are 1232 main dipole magnets installed, providing a 8.35 T field when the protons reach 7 TeV. Eight cavities with 5.5 MV/m field strength provide in total 16 MV accelerating voltage per beam. To focus the beam at the interaction points (IP), a triplet of 31 m long quadrupole magnets is installed on each side of the IP.

First LHC collisions had actually been expected after the LHC start-up event in September 2008. Operation with single proton beams was established. However, shortly after, an incident in the interconnect region between two magnets of sector 3-4 occurred [3]. After a repair phase, a new start-up is foreseen for summer 2009.

The LHC will then be operated at highest possible energies compatible with a safe operation of the machine. The timescale for commissioning the LHC to the design centre-of-mass energy of 14 TeV is currently under discussion. Instantaneous luminosities in the order of 10^{31} cm^{-1}s^{-1} can be expected in the pilot run. In the following three years, a low luminosity period with $L = 10^{33}$ cm^{-1}s^{-1} is foreseen, corresponding to $\mathcal{L} = 1.0 - 2.5$ fb^{-1} in 2010, assuming 150 days of physics running. Initially, there will be 936 bunches per beam with with 75 ns spacing and a 250 μrad crossing angle. Eventually, the nominal number of bunches is increased to 2808 with 25 ns spacing and nominal 285 μrad crossing-angle. The number of protons per bunch will stay in the order of $5 \cdot 10^{10}$.

Since the hard scattering processes in pp collisions are due to parton-parton reactions, the proton-proton luminosity and centre-of-mass energy, $\sqrt{s}$, is not fully available for physics. Figure 1 b) shows the reduction in parton luminosity at $\sqrt{s} = 10$ TeV compared to $\sqrt{s} = 14$ TeV [4]. For mass scales above 100 GeV the rate of gluon-fusion and $q\bar{q}$ induced reactions are reduced by more than 40% and 30%, respectively. Assuming 100 pb^{-1} of data in 2009, 5 million minimum bias events, 250 thousand W bosons decaying to $\ell\nu$ and 25 thousand leptonic Z decays are expected. The number of direct photons with high transverse momentum, $p_T > 25$ GeV, is expected to be in the order of 1 million and about 1000 $t\bar{t}$ events will be produced.

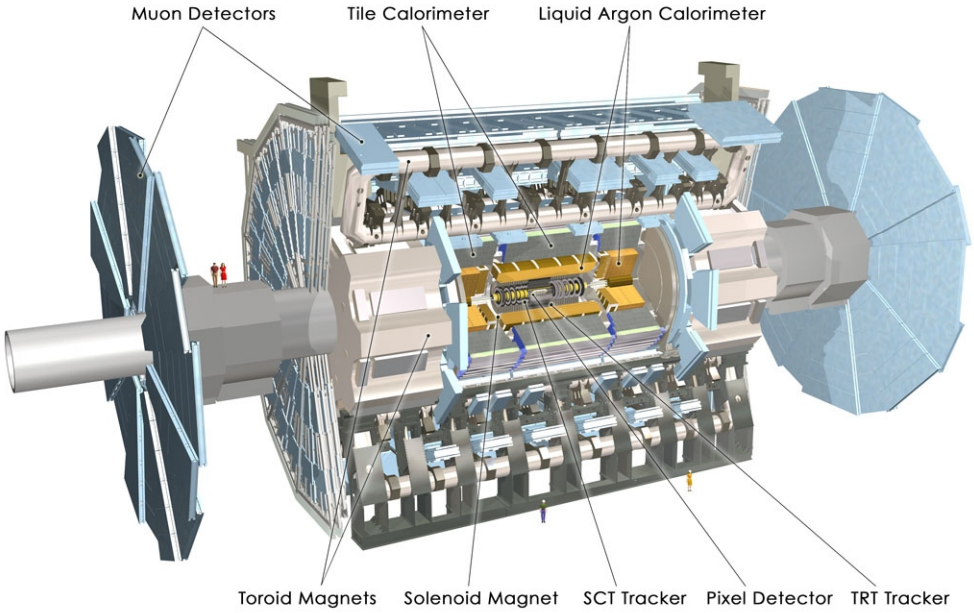

Fig. 2. Schematic view of the ATLAS detector.

3 The ATLAS detector and commissioning

The layout of the ATLAS experiment follows the well-known concepts of particle collider detectors with tracking systems for charged particles close to the interaction point, electromagnetic and hadronic calorimeters at larger distances and with muon detectors in the outermost layer. A schematic view of ATLAS is shown in Figures 2. The detector and the initial performance at the end of the construction phase is described in detail in Reference [1].

Closest to the collision vertex is the inner detector (ID) which is installed in a cylindrical superconducting solenoid of 5.5 m length and 1.15 m radius. Tracks of charged particles are bent in a 2 T magnetic field and detected by three separate tracking devices. The silicon pixel detector is composed of three barrel layers at radii between 50.5 and 122.5 mm and three endcap disks at 495 to 650 mm distance to the nominal interaction vertex. The subsequent tracking is done by the silicon tracker (SCT) which has 4 cylindrical silicon microstrip layers in the barrel section and 2×9 microstrip disks in the endcaps. The outermost silicon layer is at 514 mm radius and the most distant disk at $|z| = 2727$ mm. The combined angular coverage of the pixel and SCT reaches to pseudo-rapidity values of $|\eta| < 2.5$. The inner detector is completed by a transition radiation tracker (TRT) which uses straw tubes filled with a $Xe/CO_2/O_2$ gas mixture as active medium. The tubes provide additional 20-35 space points along the particle tracks in the fiducial volume $|\eta| < 2.0$. The combined momentum resolution for single charged tracks in the inner detector, using pixel, SCT and TRT, is

$$\frac{\sigma_{p_T}}{p_T} = \sqrt{(5 \cdot 10^{-4} p_T)^2 + 0.01^2} \tag{1}$$

in the fiducial volume $|\eta| < 2.5$. Transition radiation in the TRT is used furthermore to separate electrons and pions. For particles of 25 GeV, a $\pi^{\pm}$ rejection factor between 10 and 100 at an electron efficiency of 90% is obtained.

After installation of the inner detectors all read-out channels were thoroughly tested and dead and noisy channels identified. Overall, the number of defective pixel channels was found to be only 0.33% in 80.4 million pixels in total. Out of the 6.2 million SCT channels in barrel and endcap, 0.206% and 0.259%, respectively, were identified as problematic in the two regions.

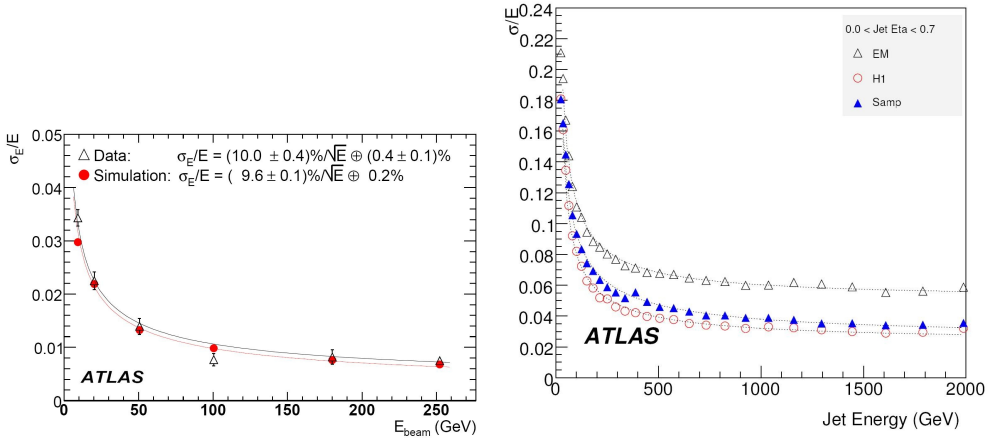

Fig. 3. a) Relative energy resolution of electrons in the electromagnetic barrel calorimeter at $|\eta| = 0.4$ from testbeam measurements compared to detector simulations. b) Energy resolution for jets reconstructed with an angular cone size $R = 0.7$ applying different calibration schemes: calibration at the electromagnetic energy scales, applying so-called "H1" calibration factors and also taking hadronic shower-depth in the different calorimeter sampling regions into account. The resolution improves more the more fine-grained calibration factors are applied.

The fraction of dead TRT channels was found to be 1.7% on the average for all 350 thousand channels. All these numbers are well below the design goals set before constructing the detectors.

The energy measurement of electrons and photons is performed in the electromagnetic calorimeter that consists of a Liquid Argon barrel and endcap calorimeter in the pseudo-rapidity ranges $|\eta| < 1.475$ and $1.375 < |\eta| < 3.2$, respectively. The calorimeter is a LAr-lead sampling calorimeter with accordion-shaped kapton electrodes and lead absorbers. The accordion structure is chosen in order to have a homogeneous energy response in ϕ without detection gaps. The barrel calorimeter has a depth of at least 22 radiation lengths, X_0, increasing to maximal 36 X_0, while the endcap provides between 24 X_0 and 38 X_0 of absorbing material.

The two halves of the LAr barrel are installed in the same cryostat as the solenoid magnet and are separated by a small 4 mm gap. The barrel electrodes are segmented in radial direction in three compartments each having different signal cell sizes. The innermost strip layer is meant to sample the beginning of the electromagnetic shower with high resolution to be able to resolve adjacent showers, for example from $\pi \rightarrow \gamma\gamma$ decays, converted photons or bremsstrahlung photons close to electron clusters. The middle layer is generally containing the peak of the electromagnetic energy deposition along a photon or electron shower, while the back layer is measuring the shower tail. The LAr calorimeter has in total about 180 thousand cells that are read out.

The calorimetry of ATLAS is completed by a hadronic tile calorimeter in the barrel $|\eta| < 1.0$ and extended barrel region $0.8 < |\eta| < 1.7$. It is built of steel as absorber and scintillating tiles are the active material. In the forward region, the LAr hadronic endcap calorimeter (HEC) and the LAr forward calorimeter (FCAL) further extend the angular coverage down to $|\eta| < 4.9$.

The obtained energy resolution for electromagnetic particles in the barrel detector is shown in Figure 3. Hadronic jets are constructed from energy deposits within typical angular cone sizes of $R = \sqrt{\Delta\eta^2 + \Delta\phi^2} = 0.7$. Figure 3 shows the energy resolution in the central detector region $|\eta| < 0.7$ for different sets of calibration factors.

The construction and installation of the ATLAS calorimeters are completed. All calorimeters were tested in detail on the surface and after installation. The fraction of non-functional readout channels is very low: 0.02% in the electromagnetic barrel and endcap, 0.09% in the HEC, and 0.23% in the FCAL. The calorimeter systems are in permanent use for electronics calibration and combined cosmic data taking since 2006.

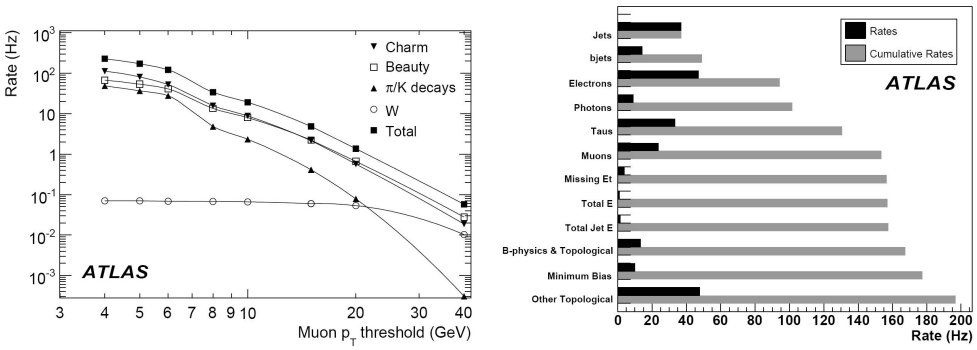

Fig. 4. a) Estimated L1 trigger rates for muons with different p_T thresholds. The contributions from the various physics processes are shown together with the total rate. b) Expected trigger rates for different physics signatures identified by the ATLAS high-level trigger. The effective output rates as well as the cumulative rates, including overlap, are shown as black and grey bars, respectively.

The outermost detector layer of ATLAS is composed of four different muon detection systems: monitored drift tubes (MDT) in barrel and endcap for the precise measurement of the muon momenta, thin-gap chambers (TGC) in the endcap for triggering, cathode-strip chambers (CSC) for the innermost endcap region, and eventually resistive plate chambers (RPC) for triggering and momentum determination in the barrel. The magnetic bending field is provided by three air-coil superconducting toroid magnets. Eight barrel toroid coils create a field of 0.15 to 2.5 T, while the endcap field is between 0.2 and 3.5 T, depending on the azimuthal and polar angle.

The angular coverage of the MDTs is $|\eta| < 2.7$ and there are more than 1000 chambers with 340 thousand channels installed. The innermost MDT layer only reaches to $|\eta| < 2.0$. CSC chambers cover this endcap region $2.0 < |\eta| < 2.7$ with high neutron background and high particle rate. The more than 500 RPC trigger chambers are installed at the middle and outer MDT layers in the fiducial region $|\eta| < 1.05$. Triggering is extended to $1.05 < |\eta| < 2.7$ in the forward region by 3588 TGC chambers. Also the installed muon systems are functional with a high fraction of properly working channels. The MDT, TGC and CSC chambers can be read-out to 99.9% and the RPC system to 99.5%.

Interesting physics events are pre-selected by the ATLAS trigger system. It is divided into three layers, where the first one (L1) is implemented in custom hardware. The second and third level triggers, L2 and Event Filter (EF), are based on software algorithms running on large PC farms. The software triggers are also called high-level triggers (HLT).

The first level trigger has two main inputs: the calorimeter trigger and the muon trigger. The calorimeter trigger identifies electron, photon and τ candidates above programmable p_T thresholds with possible isolation from other detector activities. Hadronic objects and quantities are also triggered on, like jets, $\sum E_T$ and E_T^{miss} which have to fulfil energy and multiplicity thresholds.

The muon trigger system applies fast track identification algorithms with different p_T thresholds. Figure 4 shows the expected event rate at low, initial luminosities of 10^{31} cm^{-1}s^{-1}. At a typical threshold of $p_T > 15$ GeV, used e.g. in SM measurements, the total rate is estimated to be 30 Hz, dominated by heavy quark production.

Each L1 trigger object defines a so-called region of interest (RoI) which is an angular region in η and ϕ where an interesting event feature was detected. This may be an identified particle, jet, or E_T^{miss} candidate, as well as an event property, e.g. the total sum of energy recorded in the event. The L2 algorithms are seeded from the RoI and only access data within this region, which is about 1-2% of the full event information. The L2 algorithms then search for more refined physics signatures. The last trigger level has access to the complete event data. The EF algorithms are tuned such that the final event output rate is at 200 Hz. Details of the individual rates are shown in Figure 4 for a trigger setup at $\mathcal{L} = 10^{31}$ cm^{-1}s^{-1}.

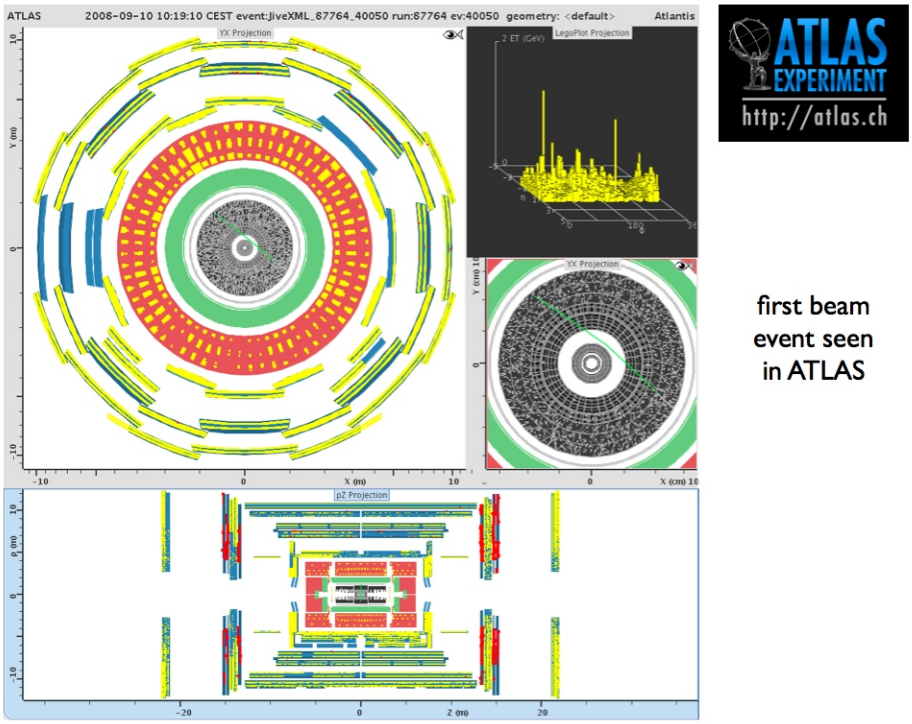

Fig. 5. First LHC beam event recorded by ATLAS.

All ATLAS detectors and trigger systems (with the only exception of the muon CSC readout) were operational at LHC start in September 2008. The very first event in ATLAS is shown in figure 5. It is the interaction of a single proton beam hitting the upstream collimator and producing a shower of particles along the beam direction in the ATLAS detector. Before and after this event, several million of cosmic ray triggers were recorded for calibration and alignment. The sub-systems are completed, commissioned and, apart from temporary and system-specific faults related to normal operation, fully functional.

4 Expectations for First Physics With ATLAS

4.1 Physics Road-map

The instantaneous LHC luminosity will increase with time such that the usage for measurements with the ATLAS detector can be divided into different stages. With $10 - 100$ pb^{-1} of data collected in the very early phase (2009), detector calibration, trigger performance studies, trigger adjustment, and material studies will be performed. Known physics processes, like Drell-Yan Z- and W-Boson production, are used as standard candles for these tasks. Table 1 summarizes some of the performance goals for e/γ energy scale and uniformity, for jet energy scale, as well as for tracking and muon alignment.

In the subsequent phase, with up to about 1 fb^{-1} of data (expected in 2010), calibration and alignment will be further refined. Here, background processes for Higgs and SUSY searches need to be studied. Inclusive searches for SUSY particles, respectively their decays, will be possible in that SUSY parameter space with sensitivity to production cross-sections down to ≈ 0.5 fb.

Once the amount of well understood data goes beyond 1 fb^{-1}, the sensitivity extends to more rare processes, like the production SM and SUSY Higgs bosons as well as heavy new particles in

Table 1. Expected ATLAS calibration and alignment performance at the start of data taking and with first data samples.

Quantity	Initial Performance	Performance With Data	Data Samples
e/γ energy scale	2%	0.1%	$Z \to e^+e^-$, $J/\psi \to e^+e^-$
e/γ uniformity	1-2%	0.7%	$Z \to e^+e^-$
jet energy scale	5-10%	1%	$W \to q\bar{q}$ in $t\bar{t}$, γ/Z + jets
tracking alignment	$10 - 50$ μm	< 10 μm	tracks, $Z \to \mu^+\mu^-$
muon alignment	$100 - 200$ μm	30 μm	inclusive muons, $Z \to \mu^+\mu^-$

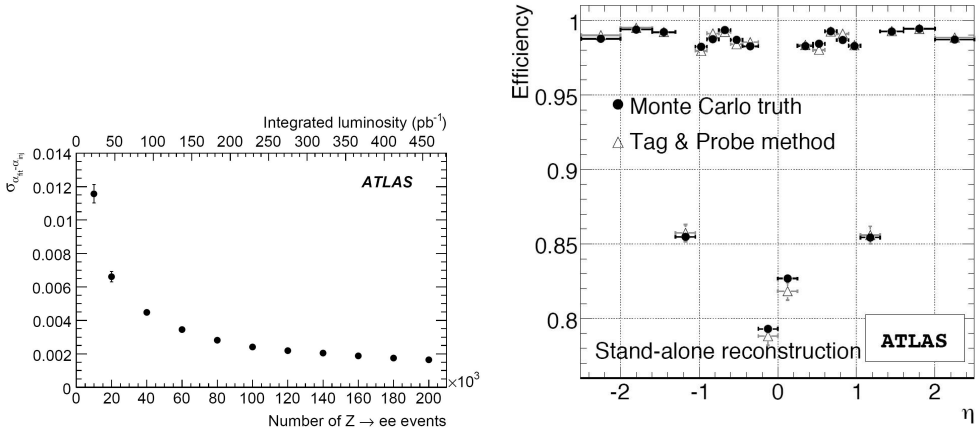

Fig. 6. a) Constant energy resolution term from long-range non-uniformities in the calorimeter as planned to be measured from the line-shape of $Z \to e^+e^-$ events. b) Muon reconstruction efficiency determined from simulated $Z \to \mu^+\mu^-$ events and the corresponding background in 100 pb^{-1} of ATLAS data. The result from the "tag&probe" method compares very well with the expectation directly derived from Monte Carlo information. The inefficiencies at $|\eta| \approx 0$ and $|\eta| \approx 1.2$ are due to the small gap between two muon barrel systems and the barrel-endcap transition region.

the TeV range. Selected expectations are summarized in the next sections. Detailed information about all topics presented here are collected in Reference [5].

4.2 Detector Performance With First Data

First LHC collision data are used to verify and improve the calibration and alignment that has already been achieved with the corresponding dedicated hardware calibration systems. As an example, $Z \to e^+e^-$ events are planned to be used to inter-calibrate the different calorimeter regions with a relative uniformity of 0.5% between regions of size $\Delta\eta \times \Delta\phi = 0.2 \times 0.4$. Together with the local uniformity obtained by cell-by-cell calibration, this is necessary to reduce the constant resolution term to below 0.7%. Figure 6 shows that only 100 pb^{-1} of data are needed to achieve this goal. The Z decay events serve also as a reference sample from which the absolute electromagnetic energy scale can be derived. Local energy scale factors are adjusted until the shape of the di-electron invariant mass distribution corresponds well to the Breit-Wigner line-shape folded with a resolution parameterisation, as expected for $Z \to e^+e^-$ production. Since the Z mass is known to 2.1 MeV from LEP measurements [6], the electron energies can be calibrated with high precision.

The $Z \to \ell^+\ell^-$ decays are also an ideal tool to measure lepton reconstruction, identification and trigger efficiencies, as well as resolutions directly from data. The events are triggered and selected by requiring a high-p_T lepton to tag the event and a second object in an invariant

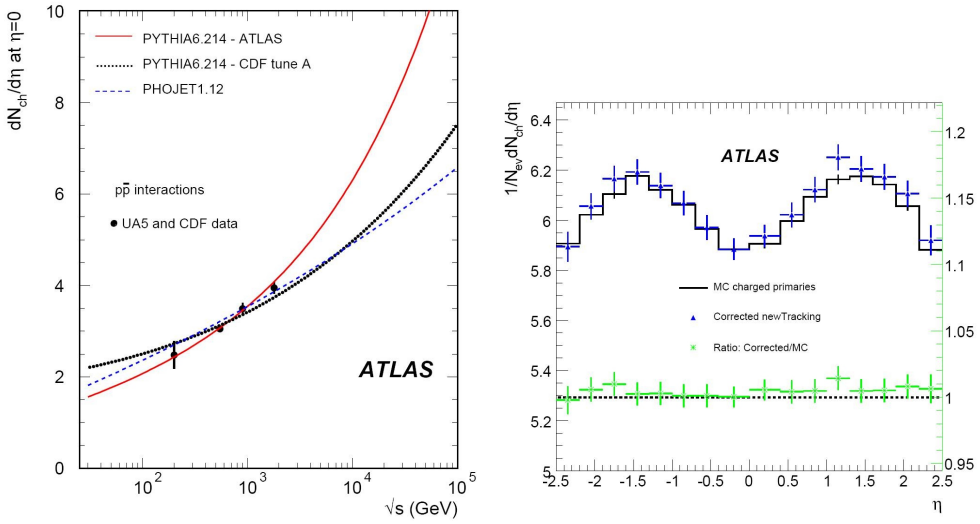

Fig. 7. a) Central charged particle density at $\eta = 0$ for non-single diffractive inelastic collisions. The lines show predictions compared to UA5 and CDF $p\bar{p}$ data. ATLAS data will be taken at $\sqrt{s} = 1.0 - 1.4 \times 10^4$ GeV. b) Expected normalized charged particle production rate corrected to non-single diffractive Monte Carlo prediction at particle level. The ratio of the simulated data sample with the prediction is also shown.

mass interval close to the Z boson mass. This object is used as a probe to derive the various efficiencies. Figure 6 shows, as an example, the muon identification efficiency, as it could be determined from 100 pb^{-1} of data. The relative background is small, less than 0.1%, and originating from $b\bar{b} \to \mu\mu$ production, $W \to \mu\nu$ and $Z \to \tau\tau$ decays, as well as $t\bar{t}$ production. Similar measurements are foreseen for electrons and taus. The results of these studies will be compared to the estimated detector performance to eventually derive systematic uncertainties.

4.3 Benchmark Processes

4.3.1 Minimum Bias

Each hard-scattering proton-proton event is accompanied by a certain number of minimum bias events, between 2 and 18 events for luminosities between 10^{33} cm^{-1}s^{-1} and 10^{34} cm^{-1}s^{-1}. The measurement of minimum bias events is therefore important for the understanding of the underlying event structure, but also as a physics process of its own. The total proton-proton cross-section can be divided into an elastic (el) and inelastic component, where the inelastic is again split into single-diffractive (sd), double-diffractive (dd), and non-diffractive (nd) contributions [7]:

$$\sigma_{tot} = \sigma_{el} + \sigma_{sd} + \sigma_{dd} + \sigma_{nd}$$

Since the minimum bias triggers are usually installed symmetrically in the forward and backward region of the detector and are operated in coincidence, the minimum bias cross-section corresponds only to the non-single-diffractive (nsd) part: $\sigma_{nsd} = \sigma_{tot} - \sigma_{el} - \sigma_{sd}$. Measurements of this process were already performed at lower centre-of-mass energies, as shown in terms of the central charged particle cross-section in Figure 7. Models like Pythia [8] and Phojet [9] describing these data extrapolate very differently to LHC energy scales. For example, in the early running phase, with luminosities of 10^{31} cm^{-1}s^{-1} and a bunch spacing of 75 ns, the rate of inelastic events is 800 kHz, and the mean number of events per bunch crossing will be 0.06.

The minimum bias trigger scintillators (MBTS) are mounted on the front face of the electromagnetic calorimeter endcaps at $2.12 < |\eta| < 3.85$. A first study is based on a trigger using

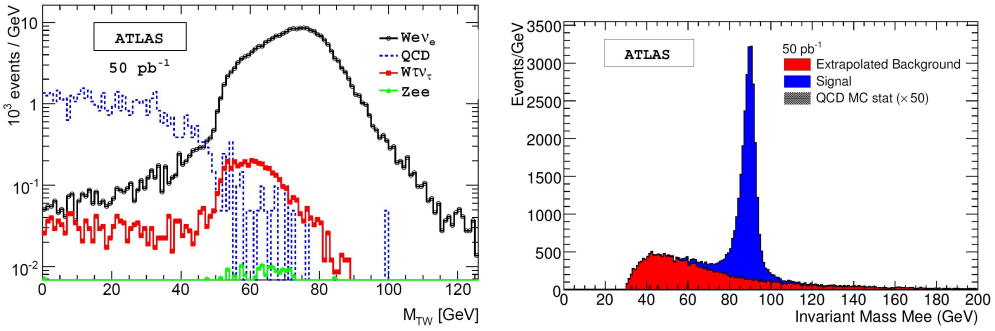

Fig. 8. a) Simulated transverse mass distribution in the $W \to e\nu_e$ channel for an integrated luminosity of 50 pb^{-1}. b) Invariant di-electron mass measured in $Z \to e^+e^-$ events and the corresponding background, again for 50 pb^{-1}.

MBTS signals, and a combination of a random beam trigger, pixel and SCT space-points at L2, and reconstructed HLT tracks. The acceptance of the proposed triggers is around 85-92% with a fraction of around 80% of non-diffractive events and about equal numbers of single and double diffractive events. In the differential cross-section measurement, tracks pointing to the nominal collision vertex with a $p_T > 105$ MeV are selected. The expected result after correcting to particle level, and after removal of reconstruction and trigger biases, is shown in Figure 7 for a sample of 75000 events, corresponding to $\mathcal{L} = 10^{-6}$ pb^{-1}. In this data set, the charged particle density will be measured with per-cent precision. Systematic uncertainties are estimated to be in the order of 8%, and originate mainly from detector misalignment and the current understanding of the Monte Carlo for the non-single-diffractive process. Backgrounds are mainly from beam-gas collisions and beam-halo events created by interactions in the upstream collimators. These can be studied in randomly triggered events, which do not contain a pp interaction. The determination of the central charged particle density will be one of the very first measurements of ATLAS.

4.3.2 W and Z Boson Production

The production of W and Z bosons is another process with high event rates at the LHC, with NNLO cross-sections of 20.5 nb [10] for $W \to e\nu_e, \mu\nu_\mu$ final states and 2.02 nb [10] for $Z \to e^+e^-, \mu^+\mu^-$ production at $\sqrt{s} = 14$ TeV. The theoretical predictions have a rather high precision of about 1% and the cross-section measurements provide stringent tests of QCD. In addition, differential rapidity distributions $d\sigma/dy$ are sensitive to parton distribution functions (PDFs) of the proton.

At low luminosities of 10^{31} cm^{-1}s^{-1}, the trigger thresholds can be rather low, $p_T > 10$ GeV, for single electron and muon signatures. Electron and muon pairs are required to pass at least $p_T > 5$ GeV and $p_T > 4$ GeV, respectively. These thresholds are approximately doubled at 10^{33} cm^{-1}s^{-1}. The selection of $W \to e\nu$ events is subsequently asking for a well identified electron reconstructed from an electromagnetic cluster in the calorimeter matched in angle to a track, such that $E_T > 25$ GeV and $|\eta| < 1.37$ or $1.52 < |\eta| < 2.4$. The pseudo-rapidity region at the barrel-endcap transition region is thus not considered. The missing transverse energy due to the neutrino has to pass $E_T^{miss} > 25$ GeV and the transverse mass $M_{\mathrm{W}}^T > 40$ GeV, defined as $M_{\mathrm{W}}^T = \sqrt{2p_T^\ell p_T^\nu (1 - \cos(\phi^\ell - \phi^\nu))}$, with the azimuthal angle $\phi^{\ell,\nu}$ of lepton and neutrino. In 50 pb^{-1} of data, 220 thousand signal events are expected. Main backgrounds are QCD jet production, followed by $W \to \tau\nu$ and $Z \to e^+e^-$ events, summing up to about 10% of the signal expectation. The transverse mass distribution is shown in Figure 8. Since QCD jet production is the primary background and has at the same time relatively large theoretical uncertainties, a data driven method is developed for its estimation. Especially the modelling of

Table 2. Expected number of signal and background events, N and B, overall selection efficiencies, $A \times \epsilon$, and cross-section measurements, σ, together with their uncertainties, for an integrated luminosity of 50 pb^{-1}. The uncertainty on N is statistical, the other sources are systematic. An overall luminosity uncertainty is not included.

Process	$N(\times 10^4)$	$B(\times 10^4)$	$A \times \epsilon$	$\delta A/A$	$\delta\epsilon/\epsilon$	σ (pb)
$W \to e\nu$	22.67 ± 0.04	0.61 ± 0.92	0.215	0.023	0.02	$20520 \pm 40 \pm 1060$
$W \to m\nu$	30.04 ± 0.05	2.01 ± 0.12	0.273	0.023	0.02	$20530 \pm 40 \pm 630$
$Z \to \mathrm{e^+e^-}$	2.71 ± 0.02	0.23 ± 0.04	0.246	0.023	0.03	$2016 \pm 16 \pm 83$
$Z \to mm$	2.57 ± 0.02	0.010 ± 0.002	0.254	0.023	0.03	$2016 \pm 16 \pm 76$

the E_T^{miss} background distribution before the final cut is important. A $\gamma + jets$ event sample, very similar to the signal process, is selected by requiring that no charged tracks are pointing to the electromagnetic cluster instead of having an angular match. Thus, the control sample has similar kinematics to the signal but *a priori* no missing energy like the background. Therefore, the background E_T^{miss} spectrum can be derived from these events and systematic uncertainties are reduced. Table 2 summarizes the event numbers, acceptances, A, and efficiencies, ϵ, as well as the prediction for the cross-section measurement in 50 fb^{-1} of data. The $W \to \mu\nu$ selection follows a similar strategy. However, the jet backgrounds are dominated by $bb \to \mu X$ events which can be rejected by requiring muon isolation from hadronic activity and impact parameter cuts. A good understanding of the detector and the underlying event is necessary. Luminosity uncertainties will be significant during initial running, but can be removed by taking ratios of cross-sections σ_W/σ_Z. This will improve once the absolute luminosity calibration with the ALFA detector [1] will be available.

The era of Standard Model parameter measurements of W boson and top quark masses at the LHC will also start already with first data. The high precision goals of $\delta M_{\mathrm{W}} \approx 15$ MeV and $\delta M_{\mathrm{t}} \approx 1$ GeV will need a detailed understanding of detector systematics, like lepton and jet energy scales. However, a first measurement with early data samples represents an interesting performance test. The precision of the W mass measurement, derived from the W transverse mass and leptonic p_T spectrum is expected to be in the order of 200 MeV with 15 pb^{-1} of data. Already at this level, the uncertainty is systematically dominated by lepton energy scale and E_T^{miss} uncertainties. These shall be studied and calibrated in $Z \to \ell\ell(+jets)$ production.

High mass lepton pairs from $Z \to \mathrm{e^+e^-}$ and $Z \to \mu^+\mu^-$ decays can be cleanly isolated from background by asking for invariant di-lepton masses close to the nominal Z boson mass. For electron final states, jet production represents the main background, while non-signal di-muons are found in $t\bar{t}$ production and $bb \to \mu\mu X$. Figure 8 and Table 2 summarize the expected results for the first ATLAS data set. Also here, the measurement is dominated by systematics, which is mainly originating from background and efficiency uncertainties in the W and Z channels, respectively.

Important insights into beyond leading-order QCD jet production can be learned by selecting explicitly $Z \to \mu^+\mu^- + jets$ signatures from the $Z \to \mu^+\mu^-$ sample (and similarly for $Z \to \mathrm{e^+e^-}$). This is interesting by itself and necessary to understand backgrounds to new particle searches. In an ATLAS study, di-muon events in the mass range 81 GeV $< m_{ee} <$ 101 GeV with isolated muons of high $p_T > 15$ GeV are selected. Jets are identified with a $\Delta R > 0.4$ with respect to the muon, a transverse momentum, $p_T > 40$ GeV, and a pseudo-rapidity range $\eta < 3.0$. The purity for $Z \to \mu^+\mu^-$ with additional 1-, 2- and 3-jets is found to be $(96.2 \pm 1.0)\%$, $(90.1 \pm 1.9)\%$, and $(89.7 \pm 3.7)\%$, respectively. The spectrum of the jets is determined and then corrected back to Monte Carlo generator level, using ALPGEN [11] as a reference. Figure 9 compares the different predictions at parton level. The actual comparison is done on hadron-level but reveals similar features: the LO prediction of PYTHIA differs from the NLO MCFM [12] and ALPGEN calculation, especially in the high jet p_T region. Figure 9 shows also the expected precision for different systematics due to jet energy scale. Initially, this scale will not be known better than 10% (with $\mathcal{L} = 1$ fb^{-1}). But with more data, a 5% precision is expected to be reached, providing sensitivity to LO vs. NLO differences.

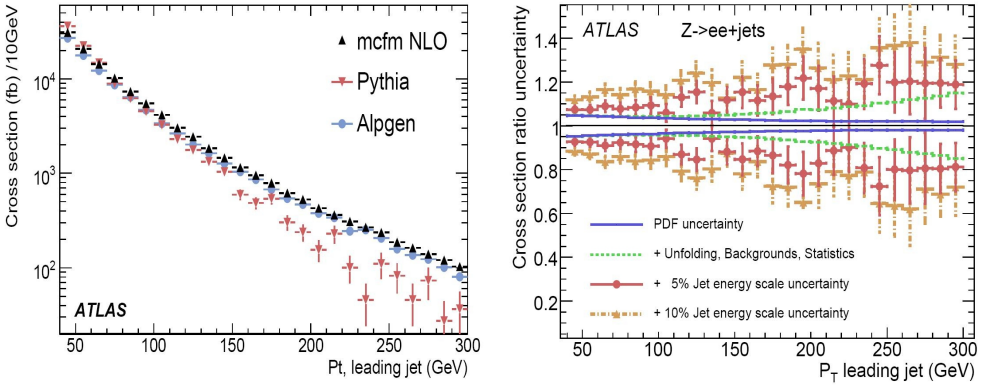

Fig. 9. a) Parton level comparison of the p_T of the leading jet in $Z \rightarrow \mu^+\mu^- + jets$ Monte Carlo samples for LO and NLO predictions. b) Systematic uncertainty on hadron level p_T of the leading jet in $Z \rightarrow e^+e^- + jets$ events for $\mathcal{L} = 1$ fb^{-1}. If the dominant jet energy scale uncertainty can be reduced below 10%, sensitivity to NLO predictions is possible.

4.3.3 Top Quark Production

The most prominent Standard Model process at the LHC is the top quark production, making the LHC a top factory. About 83000 top pairs are expected in 100 pb^{-1} [14]. They are produced through gluon fusion diagrams $gg \rightarrow t\bar{t}$ (90%) and quark annihilation $qq \rightarrow g \rightarrow t\bar{t}$ (10%). The cross-section depends on the exact value of the top quark mass, M_t, but can be calculated at NLO order including NLL soft gluon resummation. The renormalisation scale uncertainty is however non-negligible, in the order of 10% when the scale is varied by a factor of two [15].

The top quarks decay practically exclusively to $W + b$ since the CKM matrix element V_{tb} is close to unity. The $t\bar{t}$ events are therefore measured in three topologies according to the W decay final states: fully hadronic (46.2%), semi-leptonic (43.5%) and fully leptonic (10.3%). The ATLAS trigger system identifies those events by multiple signatures: high-p_T jets, isolated high-p_T electrons and muons in the leptonic channels, and multi-jets in the fully hadronic channel. Typical efficiencies normalised to the total event rate are in the order of 50%-60% for the lepton triggers with $p_T > 20 - 25$ GeV, nearly 100% for low threshold jet triggers with $p_T > 20$ GeV and about 10% for multi-jet triggers. Especially in the semi-leptonic final state there is a large redundancy.

The event selection in the single lepton channel requires a high p_T lepton of 20 GeV, $E_T^{miss} > 20$ GeV, four jets of $p_T > 20$ GeV with three jets passing $p_T > 40$ GeV. This results in combined trigger and selection efficiencies of 18.2% in the electron and 23.6% in the muon channel. Furthermore, additional kinematic cuts can be applied like W mass constraints and a top-mass window, as well as b-tagging. The latter is however considered as not applicable in very early data since it requires a thorough understanding of the ATLAS tracking. Without asking for a b-tag, the electron analysis expects a signal-to-background ratio of $N_S/N_B = 561/96$ events in 100 pb^{-1} and the muon analysis is expecting a ratio of $N_S/N_B = 755/143$. Events from $W + jet$ production represent the main background. The cross-section is extracted from a likelihood fit to the three-jet mass spectrum, as shown in Figure 10, which yields a relative precision of $\Delta\sigma/\sigma = (7(stat) \pm 15(syst) \pm 3(PDF) \pm 4(lumi))\%$ for both channels combined. The systematics are dominated by initial and final state radiation (ISR/FSR) of gluons and photons, as well as the shape of the fit function used.

In the di-lepton channel, the typical signature are two high p_T leptons, E_T^{miss} due to two neutrinos which escape detection and two high p_T b-jets. Combining ee, $e\mu$ and $\mu\mu$ channels, the signal to background ratio is $N_S/N_B = 987/228$. Here, the leptonic decays of Z and W bosons are dominating the background rate. The expected precision in 100 pb^{-1} is $\Delta\sigma/\sigma =$

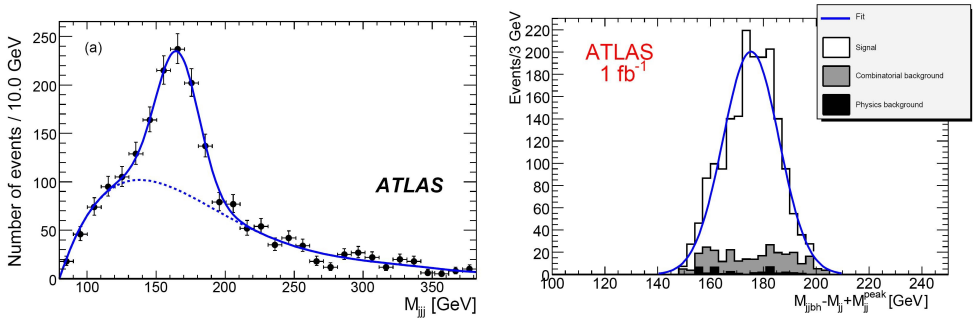

Fig. 10. a) Reconstructed top mass in the decay $t \to Wb \to jjb$ in semi-leptonic $t\bar{t}$ events for $\mathcal{L} = 100$ pb^{-1}. From this distribution the $t\bar{t}$ cross-section is determined by fitting a parameterized signal and background function to the simulated data. b) A high purity $t\bar{t}$ sample is used to measure the top quark mass. An increased width of the jjb mass due to the light jet energy scale is corrected by adding the jj mass peak-value, M_{jj}^{peak}, instead of the actual jj mass, M_{jj}, in each event. This corrects the jet energy scale uncertainty to first order. The statistical uncertainty on $M_{\rm t}$ in 1 fb^{-1} obtained in this case is 0.3 GeV.

$(4(stat)^{+5}_{-2}(syst) \pm 2(PDF) \pm 5(lumi))\%$ using a simple event counting method. In this case the jet energy scale is the main source of systematic uncertainties.

The top events themselves, and in particular the hadronic W decays, can actually be explored to calibrate the jet energy scale in data. Knowing the W mass value, the invariant jj mass spectrum can be adjusted to the expectations. Iterative energy rescaling and template methods are used. As an example, in 4000 semi-leptonic $t\bar{t}$ events from 1 fb^{-1} of simulated data, an overall scale factor of $K = M_{\rm W}^{PDG}/M_{jj} = 1.014 \pm 0.003$ is achieved reproducing well the expected value of $K_{truth} = E_{parton}/E_{jet} = 1.014 \pm 0.002$ of this specific sample.

The jet energy scale is also the main uncertainty in the determination of the top quark mass. A first study for this measurement was performed in the semi-leptonic channel. The purity of the $t\bar{t}$ sample is increased by additional kinematic constraints, e.g. on the reconstructed hadronic W mass, the b-quark energy, E_b^*, and the difference of b and W energies, $E_W^* - E_b^*$, in the top rest frame. Eventually, top, W and b purities of $(86.4 \pm 0.9)\%$, $(86.9 \pm 0.9)\%$ and $(94.0 \pm 0.6)\%$ are reached. The selection efficiency is $(0.57 \pm 0.05)\%$. From the top mass spectrum, shown in Figure 10, $M_{\rm t}$ is derived with a very good precision of 0.3 GeV, assuming $\mathcal{L} = 1$ fb^{-1}, with practically no bias. This means that the systematic uncertainties dominate, as there are: b-jet energy scale with 0.7 GeV per %, light jet energy scale 0.2 GeV per %, and ISR/FSR systematics of 0.4 GeV. The ultimate goal is therefore the reduction of the jet energy scale uncertainties to at least 1%, which is the main challenge in this measurement.

Top quarks are not only produced in pairs but also in single-top processes, where the electroweak t-channel production, $qg \to q' + t\bar{b}$ and $qb \to q't$, dominates with $\sigma_t = 246 \pm 12$ pb [16]. The Wt-channel, $gb \to b \to Wt$, is contributing with 66 ± 2 pb [17] and the s-channel, $q\bar{q}' \to W \to t\bar{b}$, with 11 ± 1 pb [16]. Single-top production is especially interesting because the cross-section is directly proportional to the CKM matrix element $|V_{tb}|^2$. The backgrounds from $t\bar{t}$, $W + bb$ and $W + jets$ are very difficult to reject. A multivariate analysis is therefore applied using variables like b-jet p_T and η, ΔR between jets and leptons, $M_{\rm W}^T$, etc.. Figure 11 shows the output of a so-called boosted decision tree (BDT) analysis [18] and the top mass spectrum for high purity events. Assuming $\mathcal{L} = 1$ fb^{-1}, a relative precision in the cross-section measurement of $\Delta\sigma/\sigma = (5.6(stat) \pm 22(syst))\%$ can be achieved. Systematic effects from b-tagging, jet energy scale, and PDFs contribute the most to the total uncertainty. Translated into a measurement of $|V_{tb}|$ one can derive $\Delta|V_{tb}|/|V_{tb}| = (11(stat + syst) \pm 4(theo))\%$, where the theory uncertainty takes strong scale and PDF dependencies into account. The s- and Wt-channels are studied as well, but a few fb^{-1} are needed to establish a signal with more than 3 standard deviations.

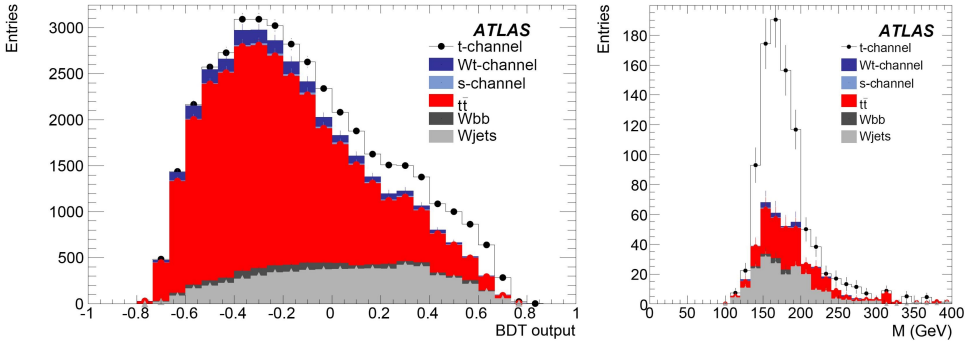

Fig. 11. a) Boosted decision tree (BDT) output for single-top signal and background. b) Leptonic top quark mass distribution applying cut on the BDT output at 0.6.

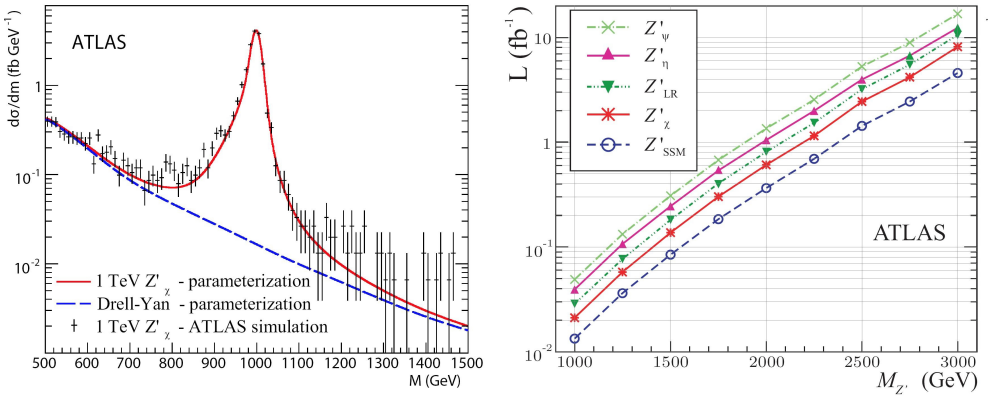

Fig. 12. a) Mass spectrum for a Z'_{χ} of 1 TeV mass decaying to e^+e^- obtained with ATLAS full simulation (dots) and the parameterization (solid line). The dashed line corresponds to the parameterization of the Drell-Yan background. b) Integrated luminosity needed for a 5 σ discovery of $Z' \rightarrow e^+e^-$ as a function of the Z' mass in various models. The curves take only statistical uncertainties into account. Systematic effects increase the necessary luminosities by 10-15%.

4.4 Searches For New Physics

4.4.1 Dilepton Resonances

Several extensions of the Standard Model predict high-mass di-lepton resonances, like grand unified theories, Technicolor, little Higgs models and large extra dimensions [19]. Experimentally, the resonances leave very similar signatures in the detector. Therefore, a few benchmark models are studied: the Sequential Standard Model, Z'_{SSM}, where the Z' couplings are assumed to follow the SM predictions, E6 models with Z'_{ψ}, Z'_{χ}, Z'_{η}, and the left-right symmetric model, Z'_{LR} [20]. Current limits from Tevatron and LEP are in the range $820-1020$ GeV [21] depending on the model. The LHC will extend the discovery reach into the multi- TeV mass range. The applied triggers and the event selection is looking for well identified electron and muon pairs. Efficiencies between 65% and 35%, decreasing with increasing masses, are estimated for the e^+e^- channel, for example. Figure 12 shows a reconstructed Z' mass peak over the irreducible Drell-Yan background $Z/\gamma^* \rightarrow e^+e^-$. The latter can be well parameterized with a smooth function and the former is assumed to follow a Breit-Wigner shape. Simulating models with different Z' masses yields the Z' mass reach, also shown in Figure 12. New bosons of 1 TeV mass can be discovered at a 5 σ significance with about 50 pb^{-1}, while in the very high-mass

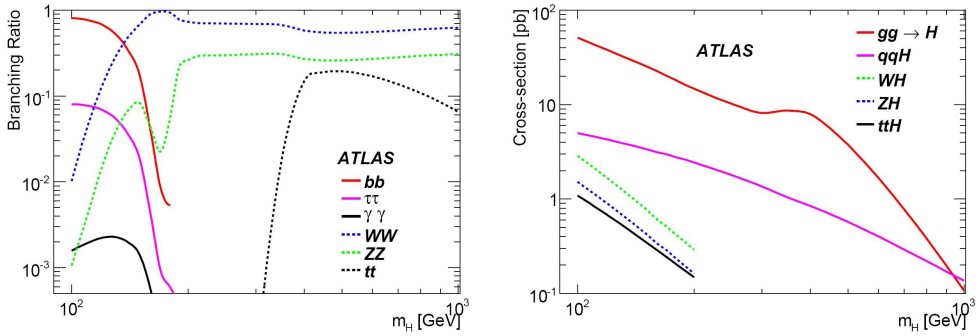

Fig. 13. a) SM Higgs branching fractions as a function of the Higgs mass, M_{H}. b) Cross-sections of different SM Higgs production modes at the LHC using NLO calculations.

region above 3 TeV more than 10 fb^{-1} are needed. The main systematic uncertainties of about 8-14% are currently from theoretical uncertainties in the Drell-Yan prediction, which may be reduced with actual measurements of this process at the LHC. Searches for W' bosons will also be performed with a similar discovery performance for the different mass ranges as the Z' searches. In early data, the sensitivity to high-mass electroweak bosons is therefore rapidly extended beyond the current exclusion limits.

4.4.2 Higgs Searches

The search for SM or SUSY Higgs bosons [22] is one of the primary goals of the LHC experiments. Present direct search results for the SM Higgs exclude masses, M_{H}, below 114.4 GeV [23] and M_{H} values around 170 GeV [24]at 95% C.L.. Global Standard Model analyses of electroweak data [25] prefer Higgs mass values below 185 GeV. In the given mass range, the SM Higgs is mainly produced through gluon-gluon fusion $gg \to H$, where subsequent $H \to \gamma\gamma$, $H \to ZZ \to 4\ell\,(\ell = e, \mu)$ and $H \to WW \to \ell\nu\ell\nu, qq\ell\nu$ decays are analysed. Figure 13 compiles the SM Higgs branching fractions and cross-sections for $\sqrt{s} = 14$ TeV. They show that the two-photon decay can only be explored up to Higgs masses of about 120 GeV, while di-boson decays start to have a significant rate below the di-boson mass threshold. The t-channel vector-boson-fusion (VBF) process has a much lower production rate. However, it has experimentally useful signatures due to the event kinematics with two forward quark jets, suppressed central jet production and a central Higgs decay. In VBF, Higgs decays to WW and $\tau\tau$ are studied. In the very low Higgs mass region, $H \to \mathrm{b\bar{b}}$ dominates, but is only detectable in Higgs-Strahlung from a $\mathrm{t\bar{t}}$ pair, leading to a $\mathrm{t\bar{t}}H \to \mathrm{t\bar{t}b\bar{b}}$ final state.

The search for $gg \to H \to \gamma\gamma$ is very challenging. The di-photon $\mathrm{q\bar{q}}, qg \to \gamma\gamma + X$ and $gg \to \gamma\gamma$ background is irreducible and dominates the spectrum together with the QCD two-jet background with misidentified jets. Only a good mass resolution helps to identify the Higgs signal, as shown in Figure 14. Since there is a significant amount of material in the ATLAS detectors in front of the LAr calorimeter, reconstruction of photon conversions is important. Some 57% of the selected events have at least one conversion at a radius smaller than 80 cm from the interaction point. The single and double track conversion reconstruction recovers those photons with efficiencies between 40% and 90% depending of the conversion radius. Also the primary vertex reconstruction is important since it influences the calculated Higgs mass. Photon triggers are efficient to more than 94% for di-photon p_T thresholds of 17 GeV. The background can be further reduced by asking for additional jets, as well as E_T^{miss}, $E_T^{miss} + \ell$, where HZ and HW associate production contributes. In the inclusive analysis signal-to-background ratios of 25.4/947 are expected for $M_{\mathrm{H}} = 120$ GeV and $\mathcal{L} = 1$ fb^{-1}.

In the $H \to ZZ \to 4\ell$ channel, high p_T electrons and muons are triggered on, and four leptons compatible with two Z decays, possibly off-shell, are selected. The continuum ZZ pro-

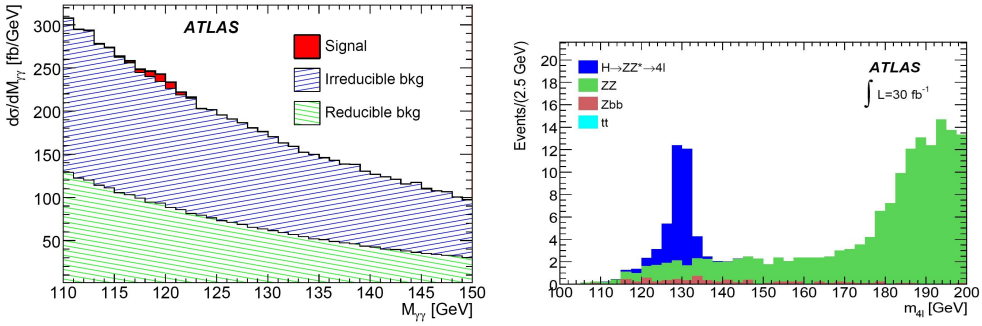

Fig. 14. a) Diphoton invariant mass spectrum after the application of cuts of the inclusive analysis, without additional requirements on jets, E_T^{miss} or leptons. b) Reconstructed 4-lepton mass for SM Higgs signal and background, which is mainly from ZZ continuum production.

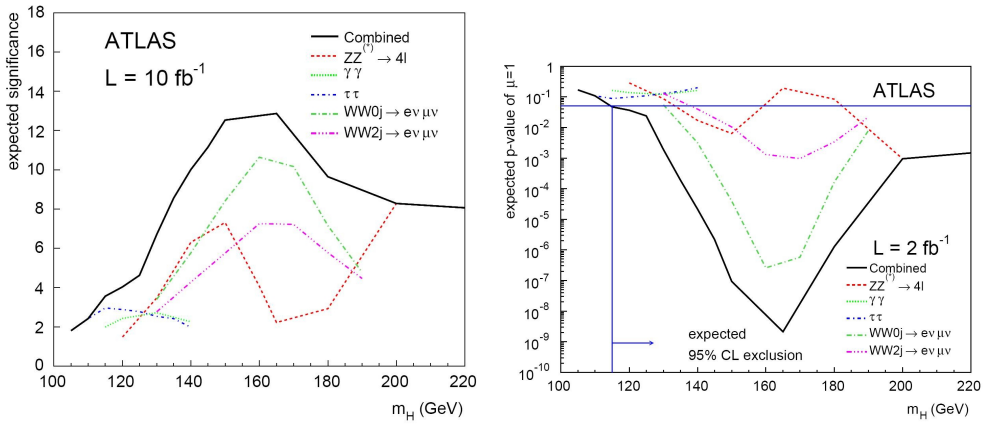

Fig. 15. a) The median discovery significance for the various Higgs decay channels and their combination for $\mathcal{L} = 10$ fb^{-1} in the low $M_{\rm H}$ region. Requiring significances above 5 translates into a possible discovery of the SM Higgs for $M_{\rm H} > 126$ GeV. b) The median p-value obtained in a profile likelihood analysis [5] for excluding a Standard Model Higgs Boson ($\mu = \sigma_{excluded}/\sigma_{SM} = 1$) for the various channels, as well as the combination for the lower mass range. Assuming $\mathcal{L} = 2$ fb^{-1} and asking for $p > 0.95$, 115 GeV $< M_{\rm H} <$ 480 GeV could be excluded.

duction represents the largest background. However, Zbb production must be carefully removed by asking for isolation of the leptons from hadronic activity in the event and lepton tracks with impact parameters that are consistent with a lepton production at the primary vertex. Also here, the mass resolution is important, which is below the 2% level for Higgs masses smaller than 200 GeV. Figure 14 shows the reconstructed mass peak in a data sample of 30 fb^{-1}. In the mass range between 150 GeV and 180 GeV the Higgs boson decays nearly exclusively to W-boson pairs. Because of the neutrinos in the $H \to WW \to \ell\nu\ell\nu, qq\ell\nu$ final states, this channel is mainly studied in VBF Higgs production, where the above mentioned search strategy is applied. Figure 15 summarizes the ATLAS expectations for the SM Higgs discovery potential with 10 fb^{-1} and the possible exclusion for 2 fb^{-1}. The most sensitive mass range is around 160 GeV. In the Higgs mass interval 114.4 GeV $< M_{\rm H} <$ 120 GeV, a discovery is most challenging and more luminosity may be needed. Also additional channels, like $Ht\bar{t}$, will then be included in the analysis. In general, with the full data set of ATLAS, the SM Higgs can however not escape detection.

In Supersymmetry, the Higgs sector is extended by a second Higgs doublet leading to in total five Higgs boson fields h, H, A, and $H^{\pm}$. In the MSSM, the physics of the Higgs bosons is mainly

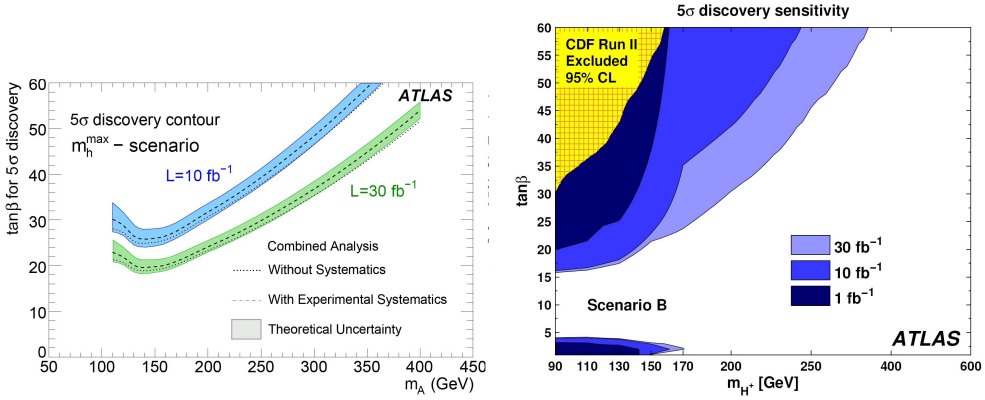

Fig. 16. a) Discovery reach in the $h/H/A \to \mu^+\mu^-$ channel. b) Discovery potential for charged Higgs bosons in the m_h^{max} scenario for different luminosities.

defined by the parameters $\tan\beta$ and m_A. The neutral Higgses $h/H/A$ decay primarily to $b\bar{b}$, $\tau^+\tau^-$ and $\mu^+\mu^-$. Searches concentrate therefore on the $\tau^+\tau^-$ and $\mu^+\mu^-$ final states, considering the production modes $gg \to h/H/A$, $gg \to h/H/A + bb$, $bb \to h/H/A$, $gb \to h/H/A + b$. The main background is from $Z \to \ell\ell$ decays with additional jets, but also from $t\bar{t}$ and the ZZ/WW processes. As an example, the expectations for the $h/H/A \to \mu^+\mu^-$ analysis are shown in Figure 16. With $\mathcal{L} = 10$ fb^{-1} in the so-called m_h^{max} scenario, the h/H/A bosons can be discovered if $\tan\beta$ values are between 25 and 60 for m_A up to 350 GeV.

ATLAS also performed studies for light charged Higgs bosons, $m_{H^\pm} < M_t$, produced through top decays $t\bar{t} \to H^+bH^-b$ and subsequent $H^\pm \to \tau\nu$ decay. In the high mass region, $H^+ \to tb$ decay is the preferred decay mode. Figure 16 shows the combined discovery sensitivity in the m_h^{max} scenario for different luminosities in the $\tan\beta - M_{H^+}$ plane, showing that it nicely extends the Tevatron parameter reach to smaller values of $\tan\beta$ and higher masses.

4.4.3 SUSY Searches

At the LHC, the supersymmetric world may however not appear at first in the Higgs sector. SUSY particle production is thus studied within the gravity and gauge mediated minimal SUSY models mSUGRA and GMSB. Benchmark scenarios are chosen to cover a wide range of experimental signatures. In both models, R-parity defined as $R = (-1)^{3B+L+2S}$ with lepton number, L, baryon number, B, and spin, S, is conserved. As a consequence, SUSY particles can only be produced in pairs and the lightest SUSY particle (LSP) is stable. This leads to typical detector signatures from the SUSY decay chains since the LSP is expected to be only weakly interacting.

Six mSUGRA models are analysed, $SU1, \ldots, SU8.1$ [5], with different values of the universal sfermion and gaugino masses at the GUT scale, m_0 and $m_{1/2}$, of the ratio of the Higgs vacuum expectation values, $\tan\beta = v_1/v_2$, of the sign of the Higgsino mass parameter, μ, and of the universal trilinear coupling, A_0, at the GUT scale. The NLO total summed SUSY cross-section varies between 6 pb ($SU6$) and 402 pb ($SU4$) [26] for the models studied. In the high SUSY mass region, the production rates for gluino and squark pairs are largest. Their decay chains lead to multi-lepton and multi-jet final states with possibly large E_T^{miss}, which is from the escaping LSP, the lightest neutralino, $\tilde{\chi}^0$. As an example, the inclusive mSUGRA analyses search for four jets of $p_T > 50$ GeV and at least one jet of $p_T > 100$ GeV, and large $E_T^{miss} > 100$ GeV. All jets and the E_T^{miss} direction should be well separated in the azimuthal angle, ϕ. The effective mass, defined as $M^{eff} = \sum_{i=1}^{4} p_T^{jet,i} + \sum_j p_T^{lep,j} + E_T^{miss}$, is highly correlated with the mass of the produced SUSY system and is asked to be larger than 800 GeV.

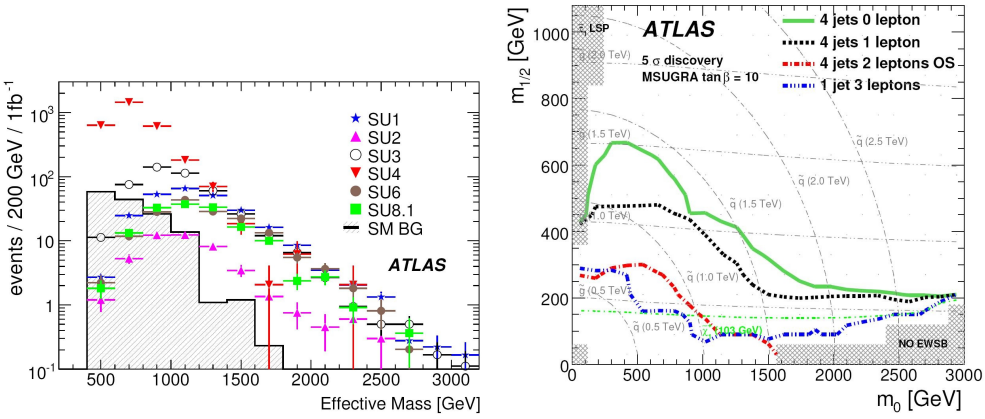

Fig. 17. a) Effective mass spectrum of simulated SUSY candidate events in the 1-lepton plus 4-jet channel. The different benchmark scenarios are marked as $SU1$-$SU8.1$. The SU4 scenario is close to the Tevatron search limits and yields the largest signal significance. b) ATLAS discovery reach from a mSUGRA parameter scan in the $m_0/m_{1/2}$ plane for $\tan\beta = 10$ and $\mathcal{L} = 1$ fb^{-1}. Systematics from jet energy and lepton scales as well as from backgrounds are included. In the most performing channels, the squark/gluino mass scale in the order of 1 TeV is probed.

The search channels with 0,1, and 2 high p_T leptons are treated separately. Opposite-sign and same-sign 2-lepton final states are again distinguished since the former is mainly from neutralino decay, $\tilde{\chi}_2^0 \to \ell^{\pm}\ell^{\mp}\tilde{\chi}_1^0$, while the latter is due to a self-conjugate Majorana-type gluino produced along the decay chain. Figure 17 shows the M^{eff} spectrum expected in the 1-lepton channel for the set of models under study. Methods to derive the background expectations from data are furthermore developed. Estimation of the E_T^{miss} and M^{eff} spectra are, for example, obtained from two-dimensional side-bands and include possible signal contamination in the procedure. Backgrounds from $Z \to \nu\nu + jets$ are studied in the process $Z \to \ell\ell + jets$ where the leptons can be removed to derive the properties of the remaining event. The 5 σ discovery reach for the analyses requiring 0, 1, or 2 opposite-sign leptons for mSUGRA with $\tan\beta = 10$ are shown in Figure 17. The plot also shows the trilepton reach with just one jet. The 0-lepton mode has the best estimated reach, close to 1.5 TeV for the smaller of the gluino or squark masses. The 1-lepton estimated reach is somewhat less, but it is more robust against QCD backgrounds.

Once the data are well understood, the SUSY decay chains will be measured with more detail. Edges in the mass spectra will be studied to derive relations between SUSY and SM particle masses from the kinematics of the different decays. One of the simplest cases is the di-lepton mass-edge, which is from the above-mentioned neutralino decay, $\tilde{\chi}_2^0 \to \ell^{\pm}\ell^{\mp}\chi_1^0$, where $m_{\ell\ell}^{edge} = m_{\tilde{\chi}_2^0} - m_{\tilde{\chi}_1^0}$. If the corresponding slepton mass is in between the $\tilde{\chi}_2^0$ and the $\tilde{\chi}_1^0$ masses, the preferred decay chain is changed to $\tilde{\chi}_2^0 \to \tilde{\ell}^{\pm}\ell^{\mp} \to \chi_1^0\ell^{\pm}\ell^{\mp}$ and the mass relation to $m_{\ell\ell}^{edge} = m_{\tilde{\chi}_2^0}\sqrt{1-(m_{\tilde{\ell}}/m_{\tilde{\chi}_2^0})^2}\sqrt{1-(m_{m_{\tilde{\chi}_1^0}/\tilde{\ell}})^2}$. Similarly, lepton+jets, squark, light stop, etc., decays are analysed. Eventually the SUSY masses can be extracted and a fit to the SUSY prediction can be performed. Table 3 summarizes the results for the $SU3$[1] benchmark point for 1 fb^{-1}. Some SUSY parameters, like the universal mass scales, are expected to be measured already with a reasonable precision at the 10% level in this scenario. The values of $\tan\beta$ and A_0 can be constrained better for a negative value of the Higgsino mass parameter μ.

[1] The $SU3$ point is in the cosmological "Bulk region", where the LSP annihilation happens through the exchange of light sleptons. It is a preferred scenario because it provides relatively large total cross-sections of 28 pb at the LHC.

Table 3. Results of a fit of the mSUGRA parameters to the ATLAS observables for the SU3 point. The mean and RMS of the distribution of the results from fits to many data-like event samples is shown. The two possible assumptions for the parameter $sign(\mu) = +1$ and $sign(\mu) = -1$ have been used, resulting in different preferred regions for the other parameters.

Parameter	$SU3$ value	fitted value	exp. unc.
	$sign(\mu) = +1$		
$\tan\beta$	6	7.4	$\pm$ 4.6
M_0	100 GeV	98.5 GeV	$\pm$ 9.3 GeV
$M_{1/2}$	300 GeV	317.7 GeV	$\pm$ 6.9 GeV
A_0	-300 GeV	445 GeV	$\pm$ 408 GeV
	$sign(\mu) = -1$		
$\tan\beta$	6	13.9	$\pm$ 2.8
M_0	100 GeV	104 GeV	$\pm$ 18 GeV
$M_{1/2}$	300 GeV	309.6 GeV	$\pm$ 5.9 GeV
A_0	-300 GeV	489 GeV	$\pm$ 189 GeV

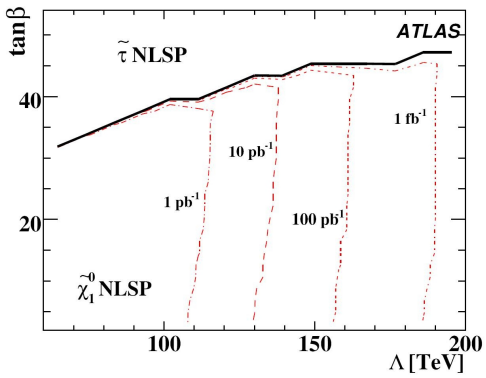

Fig. 18. GSMB discovery potential for different luminosities in the parameter space where the neutralino is the NLSP decaying to photon and gravitino.

Another MSSM scenario is evaluated in the framework of the gauge mediated SUSY breaking (GMSB) model. Here, $\tan\beta$ and the mass scale of SUSY breaking, Λ, are the main parameters [2]. Dedicated GMSB searches exploit the fact that the LSP in GMSB models is the gravitino, $\tilde{G}$. A prominent signature is the $\tilde{\chi}_1^0 \rightarrow \gamma\tilde{G}$ decay with a prompt high-energy photon. The scale of $\Lambda \approx$ 100 GeV reached currently by the Tevatron experiments [27] will be well exceeded by the ATLAS searches, as shown in Figure 18. The analysis of other GMSB models with long-lived-neutralino decays and decay signatures from long-lived heavy sleptons are pursued by ATLAS as well. These lead, for example, to decay photons which do not point to the primary vertex. Using the fine segmentation and good timing capabilities of the ATLAS calorimeter it may even be possible to eventually determine the neutralino lifetime, expected to be in the order of of $5 - 20$ ns. Studies of corresponding systematic effects are ongoing.

5 Conclusion and Outlook

The construction of the ATLAS detector is completed and all sub-systems are ready to take first LHC collision data. After an initial phase of refining the detector calibrations and understanding of the measurement performance, first measurements of Standard Model processes will be performed with $10 - 100$ pb^{-1} in 2009. Already with this amount of data, there will be

[2] after fixing the number of messenger generations, N_5, to 1.

some sensitivity to new physics beyond the Tevatron reach, e.g. to W' and Z' bosons and to SUSY signatures. With more luminosity, more and more new physics sensitivity opens up. The finding of the Higgs boson is guaranteed, if it exists, and if the Higgs mass is in a favorable range it will happen with the first $1 - 10$ fb^{-1} of data. The coming years of LHC and ATLAS physics are therefore expected to be very exciting, if not revolutionary, for elementary particle physics.

6 Acknowledgements

The work presented has been performed within the ATLAS Collaboration, and the author would like to thank the collaboration members for helpful discussions and for providing these interesting results also in graphical form.

References

1. The ATLAS Collaboration, G. Aad et al., JINST **3**, (2008) S08003.
2. L. Evans, Ph. Bryant, eds., "LHC Machine", JINST **3**, (2008) S08001.
3. LHC Project Leader Office, P. Lebrun, "Interim summary report on the analysis of the 19 September 2008 incident at the LHC", CERN EDMS Document No. 973073, October 2008.
4. W.J. Stirling, private communication.
5. The ATLAS Collaboration, "Expected Performance of the ATLAS Experiment Detector, Trigger, Physics", CERN-OPEN-2008-020.
6. C. Amsler, et al., Phys. Lett. **B 667** (2008) 1.
7. Schuler, G. A. and Sjostrand, T., Phys. Rev. **D 49**, (1994) 2257.
8. Sjostrand, T. and Mrenna, S. and Skands, P., JHEP **05** (2006) 026.
9. PHOJET manual (program version 1.05c, June 96), http://physik.uni-leipzig.de/ .eng/phojet.html.
10. K. Melnikov and F. Petriello, Phys. Rev. Lett. **96** (2006) 231803.
11. M.L. Mangano, M. Moretti, F. Piccinini, R. Pittau and A. Polosa, JHEP **0307** (2003) 001.
12. J. M. Campbell, J. W. Huston and W. J. Stirling, Rept. Prog. Phys. **70** (2007) 89.
13. DØ Collaboration, B. Abbott et al., Phys. Rev. D **61** (2000) 032004;
CDF Collaboration, A. A. Affolder et al., Phys. Rev. D **64** (2001) 052001.
14. R. Bonciani et al., Nucl., Phys. **B 529** (1998).
15. N. Kidonakis et al., Phys. Rev. **D 68** (2003) 114014.
16. J. Campbell, J. and Ellis R. K. and F. Tramontano, Phys. Rev. **D 70** (2004).
17. S. Frixione and B.R. Webber, JHEP 0206 (2002) 029;
S. Frixione et al., JHEP 0308 (2003) 007.
18. DØ Collaboration, hep-ex/080307.0739.
19. H. Georgi and S. L. Glashow, Phys. Rev. Lett. **32** (1974) 438;
K. D. Lane and E. Eichten, Phys. Lett. **B 222** (1989) 274;
N. Arkani-Hamed, A. G. Cohen, and H. Georgi, Phys. Lett. **B 513** (2001) 232;
L. Randall and R. Sundrum, Phys. Rev. Lett. **83** (1999) 3370.
20. A. Leike, Phys. Rept. 317(1999) 143.
21. D0 Collaboration, V. M. Abazov et al., Phys. Rev. Lett. **95** (2005) 091801;
CDF Collaboration, A. Abulencia et al., Phys. Rev. Lett. **96** (2006) 211801;
Particle Data Group Collaboration, W. M. Yao et al., J. Phys. **G 33** (2006) 1.
22. For a review, see for example: Djouadi, A., hep-ph/0503172, hep-ph/0503173.
23. ALEPH, DELPHI, L3 and OPAL Collaborations, Phys. Lett. **B 565** (2003) 61.
24. The TEVNPH Working Group, "Combined CDF and DØ Upper Limits on Standard Model Higgs Boson Production at High Mass ($155 - 200$ GeV/c^2) with 3 fb^{-1} of data", hep-ex/0808.0534.
25. The ALEPH, CDF, D0, DELPHI, L3, OPAL, SLD Collaborations, the LEP Electroweak Working Group, the Tevatron Electroweak Working Group, and the SLD electroweak and heavy flavour groups, "Precision Electroweak Measurements and Constraints on the Standard Model", hep-ex/0811.4682.
26. W. Beenakker, R. Hopker, M. Spira and P.M. Zerwas, Nucl. Phys. **B 492** (1997) 51;
W. Beenakker, et al., Phys. Rev. Lett. **83** (1999) 3780;
Prospino2, http://www.ph.ed.ac.uk/tplehn/prospino/.
27. The CDF Collaboration, T. Aaltonen, et al.,Phys. Rev. **D 78** (2008) 032015.